THE DEPENDENCE OF THE BARYONIC TULLY-FISHER RELATIONS ON GALAXY ROTATION VELOCITY AT VARIOUS CHARACTERISTIC RADII

Robiah Oktiavi [1]

Abstract

The effect of characteristic velocity selection on The Baryonic Tully-Fisher Relations (BTFR) can be studied in observed galaxies and simulated galaxies. Here, I use SPARC catalog and EAGLE simulation to investigate the property of BTFR and the possibility of its evolution. Through several selection criteria, 73 observed galaxies were obtained from the SPARC catalog and 207 galaxies from the EAGLE simulation for z = 0, 114 galaxies for z = 1, and 43 galaxies for z = 2.01. The fitting has been carried out using the Markov Chain Monte Carlo (MCMC) method. For SPARC data, BTFR was performed at four characteristic velocities V_{flat}, V_{max}, V_{2Reff}, and $V_{2.2Rd}$. As a result, the most tightness BTFR was shown at V_{flat} with $\sigma_{\perp} = 0.04 \pm 0.01$ which is smallest than the other. While the BTFR of EAGLE data was performed at two characteristic velocities, V_{max} for three redshifts and V_{2Reff} for z = 0. The value of V_{2Reff} was obtained by interpolating the rotation curve data at a point two effective radii and the selection of the effective radii is affected by the dominance of the baryon mass of the galaxy. In comparison to the BTFR of SPARC galaxies, the EAGLE simulation is quite good at estimating the BTFR for V_{max} and V_{2Reff} in galaxies dominated by stellar mass at z = 0. Meanwhile, BTFR V_{2Reff} for galaxies dominated by gas masses is less precise when compared to SPARC galaxies because SPARC galaxies are dominated by stellar masses. In addition, the possibility of BTFR evolution towards redshift was studied at $0 \leq z \leq 2.01$ for the EAGLE simulation, and the evidence of BTFR evolution was found towards redshift based on changes in the slope of the BTFR.

Keywords: Baryonic Tully-Fisher Relations; SPARC catalog; EAGLE simulation.

I. INTRODUCTION

Fundamental properties of galaxies, such as its velocity dispersion, luminosity, masses, and rotation velocity, can be obtained directly from observation or derived from scaling relations that describe the physical characteristics of galaxies (D'Onofrio et al. 2021). One of the commonly used methods to derive the distance parameter for late-type galaxies is the Tully-Fisher Relations (TFR), which describes the relation between luminosity (or often converted to stellar masses) and galaxy rotation velocities (Tully and Fisher, 1977). Other than determining the extragalactic distance, the TFR can be used to estimate the value of the Hubble constant (e.g. Schombert et al. 2020) and study local galaxy flows (e.g. Sandage & Tamman 1976; Tully & Fisher 1977; Source et al. 2013). Subsequently, the relation has also become a major tool to test the galaxy formation model in a Λ cold dark matter (ΛCDM) as well as alternative theories of modified Newtonian dynamics (MOND) (e.g. Milgrom 1983; Sanders 1990; McGaugh 2012). The TFR is especially interesting for low luminosity galaxies. This can be seen in the case of fitting a linear model between stellar mass and rotation velocity, where high luminosity galaxies tend to fit closely to the model while the lower luminosity galaxies scatter quite significantly from the model (McGaugh et al. 2001). This scatter is due to the assumption that the total mass of galaxy is composed of only the total stellar mass (M_*), while low luminosity galaxies are gas-rich. Therefore the total mass of each galaxy M_b or the mass of baryon should be the total of stellar mass and the mass of gas (M_g) in the galaxy. It is found that the model have less scatter for low luminosity galaxies when using $M_b = M_* + M_g$. The method describing the relations of the mass of baryons and the rotation velocities, or the Baryonic Tully-Fisher Relations (BTFR), applies in all types of spiral galaxies (Fernández Lorenzo et al. 2009). While the galaxies rotation velocity V_{rot} can be measured at different characteristic radii, and the characteristic radii chosen to measure V_{rot} can affect the properties of the BTFR, such as its slope, intercept, and intrinsic scatter. Understanding the difference in V_{rot} measurement has important implications in interpreting BTFR, as BTFR properties are used as crucial constraints on theoretical models of the

formation and evolution of galaxies. Lelli et al. (2019) investigated BTFR for rotation velocities at different characteristic radii; V_{flat} is measured along the flat part of the rotation curve, V_{max} is measured at the peak of the observed rotation curve, V_{2Reff} is measured at $2R_{eff}$ where R_{eff} is effective radii encompassing half of the galaxy luminosity, and $V_{2.2Rd}$ measured at $2.2R_d$, where R_d is the radii characterizing the profile of the exponential disc. The same work shows that the smallest scatter is found when using V_{flat}. It shows that the BTFR is naturally links to both M_b (characterized by luminosity) and dynamic mass M_{dyn} (characterized by V_{flat}) (Verheijen 2001; Noordermeer & Verheijen 2007; Ponomareva et al. 2021). This also means that galaxies with high M_b also have high M_{dyn}.

It is also possible for BTFR to evolve with redshift and it becomes a powerful tool to investigate galaxy evolution and cosmological structure formation (Ziegler et al. 2002). However, this topic is still controversial as different redshift measurements give different BTFR results. A study from Ponomareva et al. (2021), which used the MIGHTEE survey data at low redshift ($0 \leq z \leq 0.081$) did not show any indication of redshift evolution. While study of KROSS survey data at higher redshift ($z = 0.9$ and $z = 2.3$) and comparison with SPARC survey data at $z = 0$ show positive evolution for the BTFR intercept (Übler et al. 2017). Both works used observed galaxies, while study using simulated galaxies such as SIMBA simulation (Glowacki et al. 2021) at $z = 0$, 0.5 and 1, show weak redshift evolution between rotation velocity and dark matter halo mass.

This work studies how different characteristic radii affect the properties and the scatter of BTFR for observed and simulated galaxies, presents the comparison between the BTFR of the observed and simulated galaxies, and also discusses the possibility of redshift evolution for simulated galaxies. This work uses several criterias in data selection from catalogs and simulations, which will be explained further in section II (METHODS).

II. METHODS

a) Galaxy sample

Two galaxies samples are used: observation data is retrieved from *Spitzer Photometry and Accurate Rotation Curves* (SPARC) catalog (Lelli et al. 2019) and simulation data is retrieved from *Evolution and Assembly of GaLaxies and their Environments* (EAGLE) simulation (Schaye et al. 2015). From the SPARC data set, only galaxies with high quality rotation curve mark Q = 1 are used, because lower quality (Q = 2 or 3) rotation curves manifestly do not trace the equilibrium gravitational potential of the galaxy. Only galaxies with rotation velocities that have an error value not equal to zero are chosen to avoid the error while fitting. Lastly, only galaxies with baryonic mass $\geq 10^9 M_\odot$ are chosen to match the selected simulation galaxy data. These criteria result in 73 galaxies from 175 in the catalog.

In selecting data from the EAGLE simulation, galaxies with baryonic masses within the baryonic masses of SPARC data and its error range are chosen. Only galaxies with $M_g \neq 0$ are chosen. Rotationally supported galaxies are characterized by the parameter $\kappa_{co-rot} \geq 0.4$ from Correa (2017). This selection criteria result in 207 galaxies at $z = 0$, 171 galaxies at $z = 0.5$, 114 galaxies at $z = 1$, 74 galaxies at $z = 1.49$, and 43 galaxies at $z = 2.01$. This work uses galaxies with $z = 0$, 1 and 2.01 to investigate the BTFR (with 364 galaxies in total) while all 609 galaxies ($z = 0$, 0.5, 1, 1.49, and 2.01) are used to study the redshift evolution.

BTFR for SPARC data is studied for rotation velocities at all four characteristic radii (V_{flat}, V_{max}, V_{2Reff}, and $V_{2.2Rd}$). V_{flat} is measured at outer radii (which is dominated by dark matter) and represents M_{dyn} of the galaxy, and $V_{2.2Rd}$ is measured at inner radii and dominated by M_b. BTFR for EAGLE simulation was performed for V_{max} and V_{2Reff}. In this case, V_{max} is obtained from the

EAGLE database query (McAlpine et al. 2016) at z = 0, z = 1, and z = 2.01. V_{2Reff} is obtained from rotation curve data interpolation, which relies on the particle data (The EAGLE Team 2017). This work only uses V_{2Reff} from data at z = 0, as the rotation curve for EAGLE data at z ≠ 0 are not well studied yet. The interpolation was performed at a point $2R_{eff}$, with the R_{eff} taken from EAGLE are the effective radii covering half of total M_* in the galaxy, and luminosity is considered only from stellar mass. The BTFR at z = 0 for V_{max} and V_{2Reff} are compared with SPARC data to see how EAGLE simulation predicts BTFR for the SPARC data at the chosen mass range.

b) MCMC fitting

Linear fits for model is in the form:

$$\log(y) = s \log(x) + I,$$

where $y = M_b$ in $M_\odot$, x is the velocity at different characteristic radii in km/s, with s (slope) and I (intercept) being the free parameters. The maximum likelihood method was implemented by considering the orthogonal intrinsic scatter $\sigma_\perp$ as free parameters. This method is more concentrated around the best-fitting line, giving the data a higher maximum likelihood so it is preferred in a model comparison sense. To explore the posterior distributions, the simulations Markov Chain Monte Carlo (MCMC) was running using the standard affine-invariant ensemble sampler using the package **emcee** (Foreman-Mackey et al. 2013) on python. The chain was initialized with 50 random walkers and the initial value for each parameter was taken from the median of range value used by Lelli (2019). The simulations were run twice, with the second initial value being the best fit results from the first simulations. Simulations were iterated with 50000 steps each to make sure of the convergence, with 5000 burn-ints performed in the beginning.

The analysis is based on the result from each parameter of posterior distribution. Confidence Level (CL) is also considered at 68%, 90%, and 95% to see if the data is good enough to estimate the true parameter of BTFR. For EAGLE dataset, the likelihood function on scatter does not consider observed error because each data point has no error on both variables. Likelihood functions are attached in Appendix A.

## III.   RESULT AND DISCUSSION

III.A. Result

a)   BTFR of SPARC data

Table 1 shows the results of the BTFR for the SPARC data at four different characteristic radii to measure rotation velocity. All four BTFR fits show slope value in the range of 3 to 4. The least scatter seen on the BTFR using V_{flat} and the largest scatter is seen on the BTFR using $V_{2.2Rd}$.

Table 1. BTFR posterior distribution of SPARC data. First column 'x' is rotation velocity for V_{flat}, V_{max}, V_{2Reff}, and $V_{2.2Rd}$. The next columns are free parameter slopes (s), intercepts (I), and orthogonal intrinsic scatter ($\sigma_\perp$), respectively. The small scatter of $\sigma_\perp$ fulfilled by case V_{flat}.

x	s	I	$\sigma_\perp$
V_{flat}	$3.82^{+0.14}_{-0.14}$	$2.03^{+0.29}_{-0.31}$	0.04 ± 0.01
V_{max}	$3.59^{+0.13}_{-0.13}$	$2.45^{+0.28}_{-0.30}$	0.05 ± 0.01
V_{2Reff}	$3.32^{+0.13}_{-0.12}$	$3.14^{+0.27}_{-0.28}$	0.06 ± 0.01
$V_{2.2Rd}$	$3.19^{+0.13}_{-0.12}$	$3.47^{+0.26}_{-0.28}$	0.06 ± 0.01

Figure 1 shows the fitting results of BTFR at four different characteristic radii to measure rotation velocity. All four cases have similar narrow areas of CL with a small number of galaxies slightly deviating from the linear model.
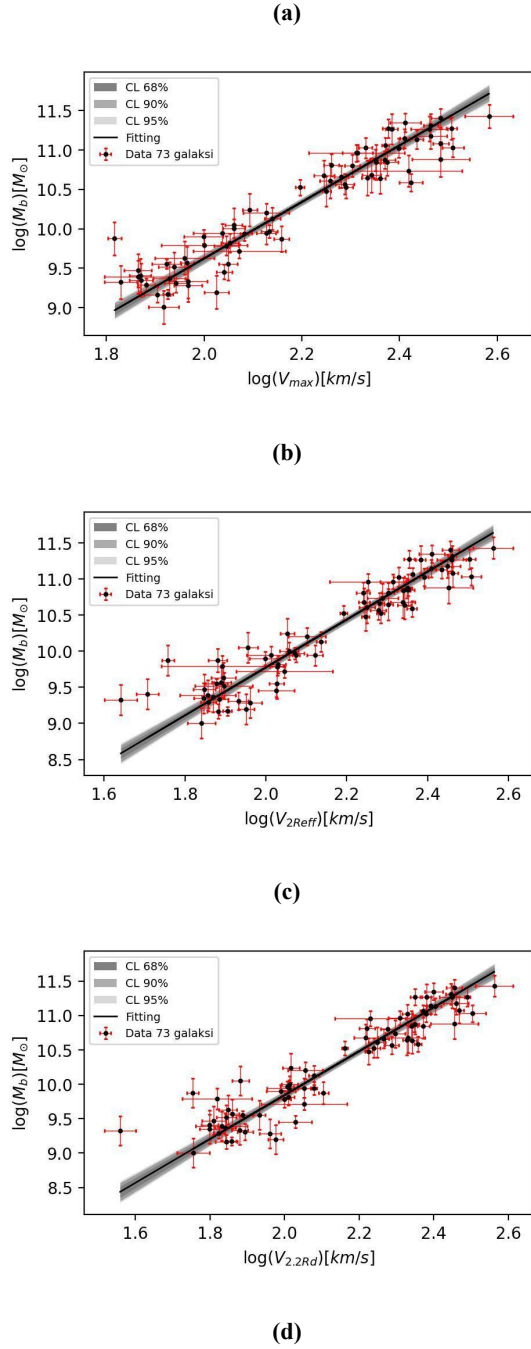
(a)

(b)

(c)

(d)
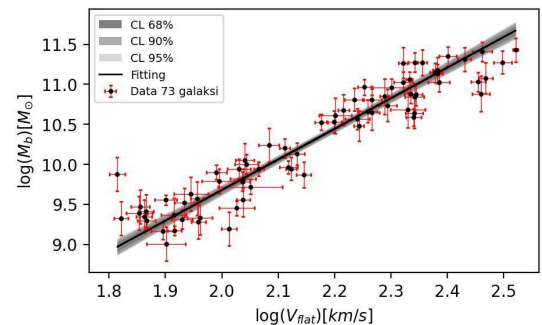
Figure 1.
BTFR plot of SPARC data for V_{flat}, V_{max}, V_{2Reff}, and $V_{2.2Rd}$ with confidence level CL 68%, CL 90%, and CL 95% respectively. Some galaxies slightly deviate from the linear model.
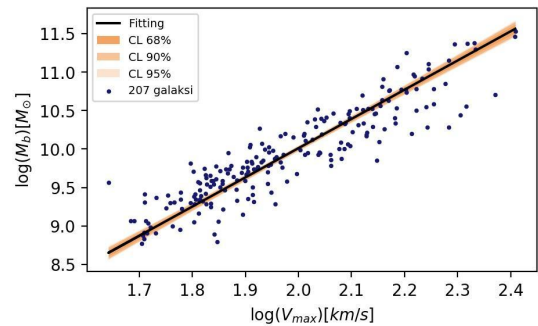
b) BTFR of EAGLE data

Table 2 shows the results of the BTFR for the EAGLE data at two different characteristic radii V_{max} at three redshifts and V_{2Reff} at redshift 0. The slopes value of cases V_{max} are in the range of 3 with $\sigma_{\perp}$ increases as the

redshifts higher. For cases V_{2Reff} the slopes and the $\sigma_{\perp}$ the value is both quite large.
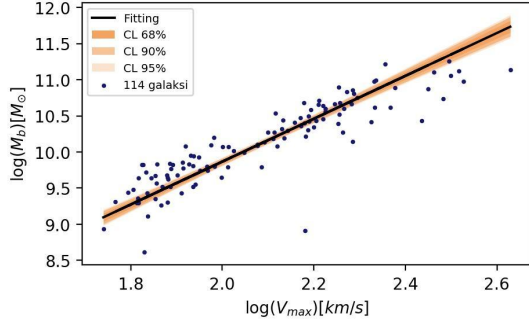
Table 2. BTFR posterior distribution of EAGLE data for V_{max} at three redshifts and V_{2Reff} at redshift 0.

| x	z	s	I	$\sigma_{\perp}$
V_{max}	0	$3.80^{+0.12}_{-0.12}$	$2.41^{+0.23}_{-0.24}$	0.07 ± 0.0031
V_{max}	1	$2.97^{+0.15}_{-0.14}$	$3.93^{+0.28}_{-0.31}$	0.09 ± 0.01
V_{max}	2.01	$3.00^{+0.29}_{-0.24}$	$3.71^{+0.51}_{-0.61}$	0.10 ± 0.01
V_{2Reff}	0	$7.54^{+1.35}_{-1.15}$	$-4.16^{+2.16}_{-2.52}$	0.20 ± 0.10

Figure 2 shows the fitting results of BTFR for V_{max} at three redshifts and V_{2Reff} at redshift 0. For V_{max}, the BTFR at three redshifts has similar narrow areas of CL and less data points deviating from the linear model. In contrast with the result for V_{2Reff} which have a large CL area and many data points that deviate from the linear model. A large scatter in the plot is seen, which will be discussed further in the next subsection (III.B. Discussion). After investigating the cause of that, the V_{2Reff} is re-interpolate and the BTFR is re-fitting. The result is shown in Figure 2. It can be seen that the CL areas become narrow and less data points deviate from the linear model. BTFR parameters from Figure 2 are also smaller than Figure 3, as can be shown in Table 3.
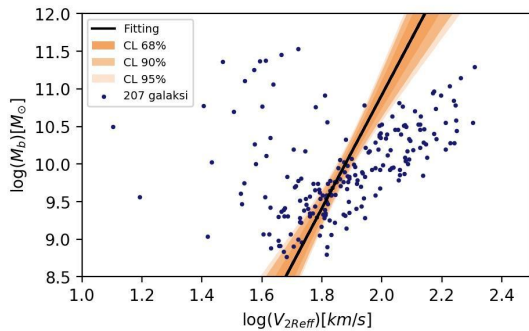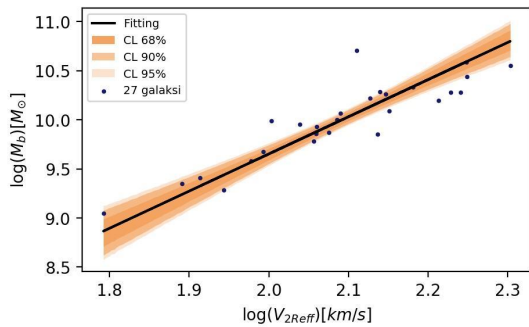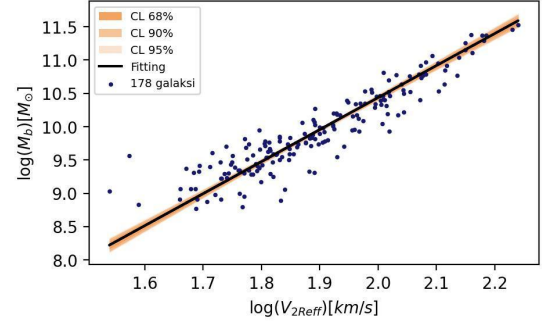

(a)

(b)
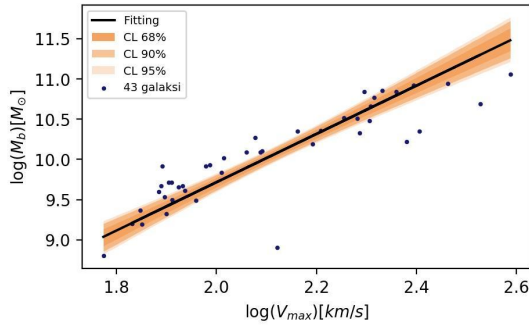
(c)

(d)

Figure 2. BTFR plot of EAGLE data for V_{max} at three redshifts and V_{2Reff} at redshift 0 with confidence level CL 68%, CL 90%, and CL 95% respectively.

(a)

(b)

Figure 3. BTFR plot of EAGLE data for V_{2Reff} at z = 0 with confidence level area of 68%, 90%, and 95%. This figure is reinterpolated and refitted from Figure 2, after choosing the different R_{eff} based on the dominating baryonic mass fraction.

Table 3. BTFR posterior distribution for V_{2Reff} of EAGLE data for stellar rich galaxies and gas-rich galaxies.

Galaxies	z	s	I	$\sigma_\perp$
Stellar rich	0	$3.79^{+0.44}_{-0.35}$	$2.08^{+0.74}_{-0.92}$	0.05 ± 0.01
Gasses rich	0	$4.80^{+0.15}_{-0.14}$	$0.83^{+0.27}_{-0.29}$	0.05 ± 0.003

c) Comparison

To compare the BTFR of observation and simulation data, both BTFR are plotted, shown in the Figure 4 for case V_{max}. It can be seen that the data points from both EAGLE and SPARC almost coincide.
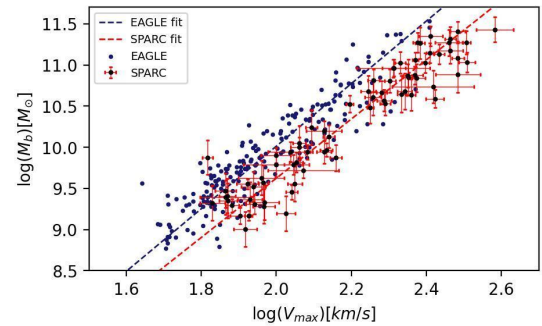

Figure 4. Comparison of BTFR using SPARC data and BTFR using EAGLE data for V_{max}. SPARC galaxies are marked in red, EAGLE galaxies are marked in blue. Linear fit is in dashed lines, red and blue for SPARC and EAGLE fits respectively.

In comparison BTFR using V_{2Reff}, for EAGLE galaxies are divided based on the dominating baryonic mass fraction. The result

is shown in Figure 5 for stellar-rich galaxies and gas-rich galaxies.
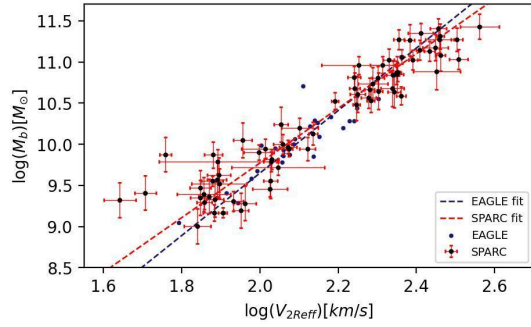
(a)
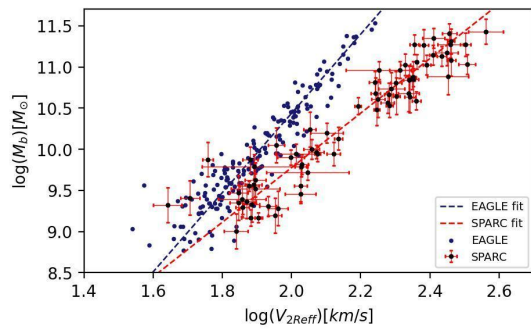
(b)

Figure 5. BTFR of SPARC data (red color), compare with BTFR of EAGLE data (blue color) for V_{2Reff} cases, (a) for stellar-rich and (b) for gasses-rich. A linear fit is given in dashed lines with corresponding color of data points.

d) BTFR evolution at EAGLE simulation

Figure 6 shows the plot of BTFR using V_{max} for galaxies at z = 0, 0.5, 1, 1.49, and 2.01 to see the possibility of evolution. It shows the difference of the galaxy's distribution at the BTFR field for each redshift.
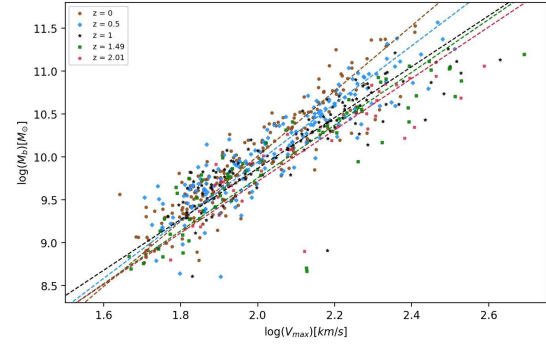

Figure 6. BTFR using V_{max} of EAGLE simulation at redshift $0 \leq z \leq 2.01$ to investigate the possibility of evolution. A linear fit is given in dashed lines with corresponding color and symbol of data points.

The posterior distribution is given by Table 4 for BTFR at each redshift.

Table 4. BTFR posterior distribution case V_{max} of EAGLE data for galaxy at $0 \leq z \leq 2.01$ to investigate the possibility of evolution. At high redshift the slopes do not change significantly but it changes towards lower redshift and the value is greatest when at z = 0.

n	z	s	I	$\sigma_{\perp}$
207	0	$3.80^{+0.12}_{-0.12}$	$2.41^{+0.23}_{-0.24}$	0.07 ± 0.0031
171	0.5	$3.39^{+0.12}_{-0.11}$	$3.16^{+0.23}_{-0.24}$	0.07 ± 0.004
114	1	$2.97^{+0.15}_{-0.14}$	$3.93^{+0.28}_{-0.31}$	0.09 ± 0.01
74	1.49	$3.08^{+0.21}_{-0.19}$	$3.60^{+0.39}_{-0.44}$	0.11 ± 0.01
43	2.01	$3.00^{+0.29}_{-0.24}$	$3.71^{+0.51}_{-0.61}$	0.10 ± 0.01

III. B. Discussion

a) BTFR of SPARC data

Result from Table 1, where least scatter is found at V_{flat} shows that BTFR correlate the M_b with V_{flat}, and agree with the results from Lelli, 2019. From the CL area in Figure 1, all four cases have similar narrow areas and this agrees with previous work by Lelli (2019), which used more samples of galaxies (150 galaxies). The results in this work indicate that all 73 galaxy samples can constrain the true parameters of BTFR quite closely, meaning it is still representative for BTFR of spiral galaxies. Another thing that can be seen in the plots from Figure 1 is the existence of

several galaxies that deviate slightly from the linear model. The galaxies that deviate from the linear model are galaxies where the baryonic mass is more dominated by gas mass in comparison to other galaxies which are dominated by stellar mass. Only a small fraction of the galaxies used are dominated by gas mass, therefore the BTFR of the SPARC data is generally representative for stellar mass-dominated galaxies

b) BTFR of EAGLE data

BTFR of EAGLE data is performed for two different rotation velocities V_{max} at z = 0, 1, and 2.01 and V_{2Reff} at z = 0. The posterior distribution map is given in Table 2. For the model using V_{max}, the slope is higher for galaxies at z = 0, indicating that for the same value of V_{max}, galaxies at z = 0 tend to have larger baryonic mass than galaxies at higher redshift. The decreasing number of data for higher redshift is the result of the selection criteria, which is for galaxies with rotational supported morphology. This indicates that galaxies tend to be more turbulent and pressure supported when the redshift is higher. From the CL area in Figure 2, the less amount of data points result in the area being wider, indicating that the true parameter is located in a larger probability area.

In the case of V_{2Reff}, there are many data points that deviate from the linear model, and the BTFR parameter values from V_{2Reff} are significantly different from predictions of different theories (ΛCDM and MOND) in the range of 3 ~ 4 (Mo et al. 1998; McGaugh 2012; Di Cintio & Lelli 2016; Desmond 2017; Sales et al. 2017; Milgrom 1983). The BTFR parameter values from V_{2Reff} have very high slope, negative intercept, and large scatter. This is because out of 207 galaxies used in the EAGLE data, 178 of them are dominated by the mass of gas (gas-rich), 27 galaxies are dominated by stellar mass (stellar-rich) with one galaxy having almost equal stellar mass and mass of gas, and 1 galaxy has equal stellar mass and mass of gas. This might indicate that the selected effective radii is affected by the mass fraction that dominates the baryonic mass of the galaxy.

EAGLE provides an effective radii for each component (stars, gas, dark matter and black holes), therefore the rotation curve data is re-interpolated using different effective radii based on the dominating fraction of baryon mass, with the two galaxies where the mass of gas and stellar mass are equal or almost equal are excluded.

The result is shown by Figure 3 and it can be seen that the BTFR becomes tighter (less scatter) as there are less data points that deviate significantly from the linear model, for both cases of BTFR (gas-rich and stellar-rich). Using this re-interpolated rotation curve, it can be seen that in the posterior distribution (Table 3), the slope value, the intercept and $\sigma_\perp$ values are smaller than before the re-interpolation.

c) Comparison

It can be concluded that the EAGLE simulation data is good enough in predicting BTFR using V_{max} in the selected mass range. The values of the error range for slopes from both EAGLE and SPARC agree with each other.

For BTFR using V_{2Reff} EAGLE simulation results are divided into the stellar-rich and gas-rich galaxies. In the case of stellar-rich, EAGLE simulation data is good enough to predict BTFR in the selected mass range. The slopes from the two data fit in the error range and as shown in Figure 5(a), the data points from both EAGLE and SPARC in the case of stellar-rich almost coincide. In the case of gas-rich galaxies, the slopes from the two data do not fit in the error range, and as shown in Figure 5(b) data points at higher V_{2Reff} have different trends. This might be caused by the difference of the dominating baryonic mass fraction, where galaxies from SPARC are overall dominated by stellar masses, so it fits better with stellar-rich EAGLE galaxies than gas-rich EAGLE galaxies.

d) BTFR evolution at EAGLE simulation

The value of parameter BTFR at each redshift indicates variability of luminosity, rotational

velocity, or both, and how M_b correlate with V_{out} in lookback time. For EAGLE galaxies at $0 \leq z \leq 2.01$, there are less galaxies with rotationally supported morphology as the redshift increases. The galaxies also show different distributions at the BTFR fields from the selected redshifts. It is shown in Figure 6 that galaxies at higher redshift tend to have more spread out distribution. At higher redshift, some galaxies have high velocity V_{max} but small baryonic mass, indicated by the the small number of galaxies with baryonic mass $M_b > 10^{11} M_\odot$, while galaxies at lower redshift have higher baryonic mass, ranging up to $M_b \geq 10^{11.5} M_\odot$.

From the posterior distribution shown in Table 4, the slope of BTFR does not change significantly in the redshift z = 2.01 to z =1, but changes significantly toward lower redshift. Galaxies with the highest slope are galaxies at z = 0. This indicates that from the selected data in this work, the BTFR does evolve toward redshifts. The possibility of BTFR evolution is important to understand the key of galaxy formation of evolution. Therefore, the evolution besides can be studied through numerical experiments, also need to be studied and compared with the observed galaxy.

IV. Conclusion

In this work, BTFR is studied through observed galaxies using SPARC catalog and simulated galaxies using EAGLE simulation. The result shows that for observed galaxies, the BTFR with least scatter is obtained for the rotational velocity at characteristic radii V_{flat} which agrees with the results of various literature. In the case of BTFR using V_{max}, the data from EAGLE and SPARC agree well with each other. In the case of BTFR using V_{2Reff}, depends on the dominating baryonic mass fraction (stellar-rich or gas-rich). For BTFR using V_{2Reff} in stellar-rich galaxies, the data from SPARC and EAGLE agree well with each other, while in gas-rich galaxies, the resulting data from SPARC and EAGLE is in the BTFR range prediction from literature but they do not agree well with each other.

Galaxies from EAGLE simulation with redshift at $0 \leq z \leq 2.01$ show the possibility of evolution toward redshift.

For better comparison, gas-rich EAGLE galaxies should be compared with observed galaxies dominated by mass of gas. It is also important to check if the BTFR with least scatter in simulated galaxies comes from the BTFR using V_{flat}, like the observed galaxies. This work checks the value from BTFR at V_{2Reff} from EAGLE galaxies at z = 0, but it is needed to check the values at different redshifts to study the possibility of evolution, along with the rotation curves at different redshifts. In EAGLE simulation, the rotation curve at $z \neq 0$ is not as well-studied yet, but it might be possible in the future. For further study of rotation curves at high redshift, more complicated computing is involved.

Acknowledgment

References

Arianna Di Cintio, Federico Lelli. (February 2016). The mass discrepancy acceleration relation in a ΛCDM context. Monthly Notices of the Royal Astronomical Society: Letters, 456(1), L127–L131. https://doi.org/10.1093/mnrasl/slv185

Correa, C. A. and 7 colleagues. (2017). The relation between galaxy morphology and colour in the EAGLE simulation. Monthly Notices of the Royal Astronomical Society, 472, L45–L49. https://doi.org/10.1093/mnrasl/slx133

D'Onofrio, Mauro, et al. (2021). Past, Present, and Future of the Scaling Relations of Galaxies and Active Galactic Nuclei. Frontiers in Astronomy and Space Sciences.

E. Noordermeer , M. A. W. Verheijen. (2007). The high‑mass end of the Tully–Fisher relation, Monthly Notices of the Royal Astronomical Society, 381(4), 1463–1472.

https://doi.org/10.1111/j.1365-2966.2007.12369.x

Fernández Lorenzo, M., Cepa, J., Bongiovanni, A., Castañeda, H., Pérez García, A. M., Lara-López, M. A., Sánchez-Portal, M. (2009, March). Evolution of the optical Tully-Fisher relation up to z = 1.3. Astronomy and Astrophysics, 496(2), 389-397. https://doi.org/10.1051/0004-6361/200811178

Foreman-Mackey, D., Hogg, D. W., Lang, D., Goodman, J. (2013). emcee: The MCMC Hammer. Publications of the Astronomical Society of the Pacific, 125, 306. https://doi.org/10.1086/670067

Glowacki, M., Elson, E., & Davé, R. (2021, November). The redshift evolution of the baryonic Tully-Fisher relation in SIMBA. Monthly Notices of the Royal Astronomical Society, 507(3), 3267-3284. https://doi.org/10.1093/mnras/stab2279

Harry Desmond. (November 2017), The scatter, residual correlations and curvature of the SPARC baryonic Tully–Fisher relation, Monthly Notices of the Royal Astronomical Society: Letters, 472(1), L35–L39, https://doi.org/10.1093/mnrasl/slx134

H. J. Mo and others (April 1998), The formation of galactic discs, Monthly Notices of the Royal Astronomical Society, 295(2), 319–336. https://doi.org/10.1046/j.1365-8711.1998.01227.x

Laura V. Sales and others, (January 2017), The low-mass end of the baryonic Tully–Fisher relation, Monthly Notices of the Royal Astronomical Society, 464(2), 2419–2428. https://doi.org/10.1093/mnras/stw2461

Lelli, F., McGaugh, S. S., Schombert, J. M., Desmond, H., Katz, H. (2019). The baryonic Tully-Fisher relation for different velocity definitions and implications for galaxy angular momentum. Monthly Notices of the Royal Astronomical Society, 484, 3267–3278. https://doi.org/10.1093/mnras/stz205

McAlpine, S. and 18 colleagues. (2016). The EAGLE simulations of galaxy formation: Public release of halo and galaxy catalogs. Astronomy and Computing, 15, 72–89. https://doi.org/10.1016/j.ascom.2016.02.004

McGaugh, S. S. (2005, October). The Baryonic Tully-Fisher Relation of Galaxies with Extended Rotation Curves and the Stellar Mass of Rotating Galaxies. The Astrophysical Journal. 632(2), 859-871. https://doi.org10.1086/432968

McGaugh, S. S. (2012, February). The Baryonic Tully-Fisher Relation of Gas-rich Galaxies as a Test of ΛCDM and MOND. The American Astronomical Society. 143(2), 40. https://doi.org/10.1088/0004-6256/143/2/40

McGaugh, S. S., Schombert, J. M., Bothun, G. D., de Blok, W. J. G. (2000). The Baryonic Tully-Fisher Relation. The Astrophysical Journal, 533, L99–L102. https://doi.org/10.1086/312628

Milgrom, M. (1983b, July). A modification of the Newtonian dynamics - Implications for galaxies. The Astrophysical Journal. 270, 371-383. https://doi.org/10.1086/161131

Ponomareva, A. A., Verheijen, M. A. W., Papastergis, E., Bosma, A., Peletier, R. F. (2018). From light to baryonic mass: the effect of the stellar mass-to-light ratio on the Baryonic Tully-Fisher relation. Monthly Notices of the Royal Astronomical Society, 474, 4366–4384. https://doi.or/10.1093/mnras/stx3066

Sandage, A., & Tammann, G. A. (1976). Steps toward the Hubble constant. VII. Distances to NGC 2403, M101, and the Virgo cluster using 21 centimeter line widths compared with optical methods: the global value of H0. The Astrophysical Journal, 210, 7-24. https://doi.org/10.1086/154798

Sanders, R. H. (1990). Mass discrepancies in galaxies: dark matter and alternatives. The Astronomy and Astrophysics Review, 2(1), 1-28. https://doi.org/10.1007/BF00873540

Schaye, J. and 21 colleagues. (2015). The EAGLE project: simulating the evolution and

Indonesia Research and Innovation Fair

assembly of galaxies and their environments. Monthly Notices of the Royal Astronomical Society, 446, 521–554. https://doi.org/10.1093/mnras/stu2058

Schombert, J., McGaugh, S., & Lelli, F. (2020). Using the Baryonic Tully-Fisher Relation to Measure H_0. The Astronomical Journal, 160(2), 71. https://doi.org/10.3847/1538-3881/ab9d88

Sorce, J. G., Courtois, H. M., Tully, R. B., Seibert, M., Scowcroft, V., Freedman, W. L., . . . Rigby, J. (2013). Calibration of the Mid-infrared Tully-Fisher Relation. The Astrophysical Journal, 765(2), 94. https://doi.org/10.1088/0004-637X/765/2/94

The EAGLE team. (2017). The EAGLE simulations of galaxy formation: Public release of particle data. arXiv e-prints. https://doi.org/10.48550/arXiv.1706.09899

Tully, R. B., Fisher, J. R. (1977). A new method of determining distances to galaxies. Astronomy and Astrophysics, 54, 661–673.

Übler, H. and 26 colleagues. (2017). The Evolution of the Tully-Fisher Relation between z ~ 2.3 and z ~ 0.9 with KMOS 3D. The Astrophysical Journal, 842. https://doi.org/10.3847/1538-4357/aa7558

Verheijen, M. A. W. 2001. The Ursa Major Cluster of Galaxies. V. H I Rotation Curve Shapes and the Tully-Fisher Relations. The Astrophysical Journal, 563, 694–715. https://doi.org/10.1086/323887

Ziegler, B. L., Böhm, A., Fricke, K. J., Jäger, K., Nicklas, H., Bender, R., . . . Sutorius, E. (2002). The Evolution of the Tully-Fisher Relation of Spiral Galaxies. The Astrophysical Journal, 564(2), L69-L72. https://doi.org/10.1086/338962

Appendix A: fitting methods

The likelihood function used are following equation from Lelli 2019 given by:

$$\ln(L) = -\sum_i^N \ln\left(\sqrt{2\pi}\delta_{\perp,i}\right) - \sum_i^N \frac{\Delta_{\perp,i}^2}{2\delta_{\perp,i}^2},$$

with the minimum distance between (x_i, y_i) and the best-fitting line is:

$$\Delta_{\perp,i} = \sqrt{\left(x_i - \frac{x_i + ay_i - ab}{a^2+1}\right)^2 + \left(y_i - b - a\frac{x_i + ay_i - ab}{a^2+1}\right)^2}$$

and total perpendicular scatter is given by:

$$\delta_{\perp,i} = \sqrt{\left(1 - \frac{\Delta_{\perp,i}^2}{\Delta_{y,i}^2}\right)e_{xi}^2 + \frac{\Delta_{\perp,i}^2}{\Delta_{y,i}^2}e_{yi}^2 + \sigma_\perp^2},$$

Where e_{xi} and e_{xi} each are error on data points x_i and y_i, $\sigma_\perp$ is orthogonal intrinsic scatter as free parameter, and $\Delta_{y,i}$ is given by:

$$\Delta_{y,i} = y_i - (ax_i + b)$$